Generation of 2-Dimensional Projections of Hyper-Ellipsoids Describing an Energy-Constrained Reachable Set of Forced Periodic Trajectories in the CR3BP

Matthew Bryan

M.Eng. Report

Preface

For my report, I contributed to the working paper "Generation of Energy-Optimal Low-Thrust Forced Periodic Structures in the CR3BP," authored by Colby Merrill, Jackson Kulik, and Dmitry Savransky. I wrote the appendix of the paper, which includes two sections describing my work during my M. Eng. project. The first section describes a process utilized for projecting 6D hyper-ellipsoids representing the energy-constrained reachable set of forced periodic trajectories into 2D space. The second section describes a process for specifying the boundaries of a projection of a reachable set using tangent lines between consecutive ellipsoidal projections. I developed code throughout my M. Eng. project that implemented these processes and produced figures included in the appendix. The mathematical definition of the energy-constrained reachable set and an explanation of a set's associated hyper-ellipsoid is described in the sections prior to the appendix. The entire paper is included in the remainder of this document. The material outside of the appendix was authored by Merrill, Kulik, and Savransky.

(Preprint) AAS 24-206

GENERATION OF ENERGY-OPTIMAL LOW-THRUST FORCED PERIODIC STRUCTURES IN THE CR3BP

Colby C. Merrill*, Jackson Kulik†, Dmitry Savransky‡

In this work, we investigate trajectories that require thrust to maintain periodic structure in the circular restricted three-body problem (CR3BP). We produce bounds in position and velocity space for the energy-constrained reachable set of initial conditions. Our trajectories are energy-optimal and analyzed via linear analysis. We provide validation for our technique and analyze the cost of deviating in various directions to the reference. For our given reference, we find that it is relatively expensive to decrease perilune distance for orbits in the Earth-Moon system.

INTRODUCTION

Uncontrolled, periodic structures in the circular restricted three-body problem (CR3BP) have been well-studied and are often exploited in spacecraft operations. There exist families of these periodic structures centered around the five equilibrium Lagrange points in a three-body system. Of particular interest are periodic structures around the L1 and L2 points, as these orbits have historically been used by spacecraft in the Earth-Sun system and are planned for use in the Earth-Moon system.

A constant perturbation applied to the CR3BP (e.g., a constant acceleration provided by low thrust propulsion), will shift the equilibrium points and allow areas beyond the natural space to be exploited.[1–5] Because the equilibrium points have been shifted, the periodic structures around the equilibria will be shifted as well.[6] Many previous studies have primarily focused on constant, low thrust trajectories[4–8] or optimal control in proximity of the shifted equilibria.[9] Other related work exists that focuses on forced circumnavigation or controlled loitering trajectories relative to a spacecraft on some reference orbit in the CR3BP.[10] In this work, we also investigate optimally controlled trajectories relative to a reference orbit. However, the emphasis here is on developing and characterizing a catalog of forced periodic orbits (trajectories that begin and end at the same state) under control rather than on the relative motion of two real satellites. Additionally, the lens through which we examine optimally controlled trajectories in the vicinity of a reference orbit leverages the analytical aspects of techniques from relative reachable set theory to provide a lower fidelity but more holistic view of optimally controlled trajectories near a reference orbit. We refer to these trajectories as forced periodic structures. While not periodic in the natural dynamics, these trajectories expand available options for satellite orbits in the CR3BP beyond naturally periodic or quasi-periodic structures.

*PhD Candidate, Sibley School of Mechanical and Aerospace Engineering, Cornell University, Ithaca, NY 14853, USA
†Assistant Professor, Mechanical and Aerospace Engineering Department, Utah State University, Logan, UT 84322, USA
‡Associate Professor, Sibley School of Mechanical and Aerospace Engineering, Cornell University, Ithaca, NY 14853, USA

METHODS

As an initial investigation into this problem, we make use of the linearized model of energy-optimal control and approximate the energy cost of optimal forced periodic structures near a naturally periodic orbit about the L2 point in the Earth-Moon system. This periodic orbit will serve as a reference trajectory for our spacecraft and we will work to understand how small perturbations in the initial and final state from this reference trajectory affect the cost of control.

The Energy-Limited Reachable Set

Here, we are interested in finding the reachable set of states for our system in the energy-constrained problem. This formalism is based on the work in Kulik et al., 2024,[11] where it is expanded upon further. We specialize results from this work to the context of forced periodic structures. We assume a dynamical system of the form

$$\frac{\mathrm{d}\mathbf{x}}{\mathrm{d}t} = \mathbf{F}(\mathbf{x}) + \begin{bmatrix} \mathbf{0}_{3\times 1} \\ \mathbf{u} \end{bmatrix} \tag{1}$$

where the state vector $\mathbf{x} \in \mathbb{R}^6$ is defined by stacking the position and velocity vectors $\mathbf{x} = [\mathbf{r}^T, \mathbf{v}^T]^T$ and $\mathbf{u}$ is the control acceleration vector. In our system, $\mathbf{F}(\mathbf{x})$ gives the natural dynamics for the third body in the "canonical rotating frame" of the CR3BP

$$\mathbf{F}(\mathbf{x}) = \begin{bmatrix} v_x \\ v_y \\ v_z \\ 2v_y + x - (1-\mu^*)\frac{x+\mu^*}{R_1^3} - \mu^*\frac{x-1+\mu^*}{R_2^3} \\ -2v_x + y - (1-\mu^*)\frac{y}{R_1^3} - \mu^*\frac{y}{R_2^3} \\ -(1-\mu^*)\frac{z}{R_1^3} - \mu^*\frac{z}{R_2^3} \end{bmatrix} \tag{2}$$

where x, y, and z are the components of the spacecraft's position vector, $\mathbf{r}$, and v_x, v_y, and v_z are the components of the spacecraft's velocity vector, $\mathbf{v}$. The distances of the third body with respect to the primary and secondary are defined as R_1 and R_2, respectively, and are evaluated as

$$R_1 = \sqrt{(x+\mu^*)^2 + y^2 + z^2} \tag{3}$$

$$R_2 = \sqrt{(x-1+\mu^*)^2 + y^2 + z^2} \tag{4}$$

where $\mu^* = m_2/(m_1+m_2)$ is the mass parameter of the system. Defining a quadratic cost function of the form

$$J = \frac{1}{2}\int_{t_0}^{t_f} ||\mathbf{u}||^2 dt \tag{5}$$

the optimal control from one state to another is given by solving a two-point boundary value problem associated with a system of ordinary differential equations. These equations have twice as many dimensions as the state of the original system and are given by

$$\frac{\mathrm{d}\mathbf{x}}{\mathrm{d}t} = \mathbf{F}(\mathbf{x}) + \begin{bmatrix} \mathbf{0}_{3\times 1} \\ \mathbf{u} \end{bmatrix} \tag{6}$$

$$\frac{\mathrm{d}\boldsymbol{\lambda}}{\mathrm{d}t} = -\left(\frac{\partial \mathbf{F}(\mathbf{x})}{\partial \mathbf{x}}\right)^T \boldsymbol{\lambda} \tag{7}$$

$$\mathbf{u} = -\boldsymbol{\lambda}_{\boldsymbol{v}} \tag{8}$$

where $\boldsymbol{\lambda_v}$ is the velocity costate vector given by the last three elements of the costate vector.[12] J can then be written in terms of the velocity costate vector as

$$J = \frac{1}{2}\int_{t_0}^{t_f} \boldsymbol{\lambda}_{\boldsymbol{v}}^T \boldsymbol{\lambda_v} dt \tag{9}$$

The augmented state is given by stacking the states and costates

$$\mathbf{y} = \begin{bmatrix} \mathbf{x} \\ \boldsymbol{\lambda} \end{bmatrix} = \begin{bmatrix} \mathbf{r} \\ \mathbf{v} \\ \boldsymbol{\lambda}_r \\ \boldsymbol{\lambda_v} \end{bmatrix} \tag{10}$$

where $\mathbf{r}$ is the position vector from the origin to the spacecraft, $\mathbf{v}$ is the velocity of the spacecraft, and $\boldsymbol{\lambda}$ are the six costates. The state transition matrix (STM) associated with the augmented state vector and its dynamics yields a linear approximation of perturbations to the final augmented state $\delta\mathbf{y}(t_f)$ at some final time, t_f, as a function of deviations in the initial augmented state:

$$\delta\mathbf{y}(t_f) = \begin{bmatrix} \delta\mathbf{r}(t_f) \\ \delta\mathbf{v}(t_f) \\ \delta\boldsymbol{\lambda}_r(t_f) \\ \delta\boldsymbol{\lambda_v}(t_f) \end{bmatrix} \approx \boldsymbol{\Phi}(t_f, t_0)\delta\mathbf{y}_0 = \begin{bmatrix} \boldsymbol{\Phi}_{\mathbf{x}}^{\mathbf{x}} & \boldsymbol{\Phi}_{\boldsymbol{\lambda}}^{\mathbf{x}} \\ \boldsymbol{\Phi}_{\mathbf{x}}^{\boldsymbol{\lambda}} & \boldsymbol{\Phi}_{\boldsymbol{\lambda}}^{\boldsymbol{\lambda}} \end{bmatrix} \delta\mathbf{y}_0 = \begin{bmatrix} \boldsymbol{\Phi}_{\mathbf{r}}^{\mathbf{r}} & \boldsymbol{\Phi}_{\mathbf{v}}^{\mathbf{r}} & \boldsymbol{\Phi}_{\boldsymbol{\lambda}_r}^{\mathbf{r}} & \boldsymbol{\Phi}_{\boldsymbol{\lambda}_v}^{\mathbf{r}} \\ \boldsymbol{\Phi}_{\mathbf{r}}^{\mathbf{v}} & \boldsymbol{\Phi}_{\mathbf{v}}^{\mathbf{v}} & \boldsymbol{\Phi}_{\boldsymbol{\lambda}_r}^{\mathbf{v}} & \boldsymbol{\Phi}_{\boldsymbol{\lambda}_v}^{\mathbf{v}} \\ \boldsymbol{\Phi}_{\mathbf{r}}^{\boldsymbol{\lambda}_r} & \boldsymbol{\Phi}_{\mathbf{v}}^{\boldsymbol{\lambda}_r} & \boldsymbol{\Phi}_{\boldsymbol{\lambda}_r}^{\boldsymbol{\lambda}_r} & \boldsymbol{\Phi}_{\boldsymbol{\lambda}_v}^{\boldsymbol{\lambda}_r} \\ \boldsymbol{\Phi}_{\mathbf{r}}^{\boldsymbol{\lambda}_v} & \boldsymbol{\Phi}_{\mathbf{v}}^{\boldsymbol{\lambda}_v} & \boldsymbol{\Phi}_{\boldsymbol{\lambda}_r}^{\boldsymbol{\lambda}_v} & \boldsymbol{\Phi}_{\boldsymbol{\lambda}_v}^{\boldsymbol{\lambda}_v} \end{bmatrix} \delta\mathbf{y}_0 \tag{11}$$

where $\delta\mathbf{y}_0 = \delta\mathbf{y}(t_0)$ is the perturbed initial state and $\boldsymbol{\Phi}(t_f, t_0)$ is a time-varying STM associated with the augmented state, reference trajectory, and initial and final times. We adopt the notation

$$\boldsymbol{\Phi}_{\mathbf{a}}^{\mathbf{b}}(t, t_0) = \frac{\partial \mathbf{b}(t)}{\partial \mathbf{a}(t_0)} \tag{12}$$

If the time dependence of an STM is omitted in this paper, it indicates that the STM corresponds to a full period (i.e., $\boldsymbol{\Phi}(t_f, t_0) = \boldsymbol{\Phi}$). $\delta\boldsymbol{\lambda_v}(t)$ at all times may be evaluated as

$$\delta\boldsymbol{\lambda_v}(t) = \boldsymbol{\Phi}_{\mathbf{y}}^{\boldsymbol{\lambda}_v}(t, t_0)\delta\mathbf{y}_0 = \begin{bmatrix} \boldsymbol{\Phi}_{\mathbf{r}}^{\boldsymbol{\lambda}_v}(t, t_0) & \boldsymbol{\Phi}_{\mathbf{v}}^{\boldsymbol{\lambda}_v}(t, t_0) & \boldsymbol{\Phi}_{\boldsymbol{\lambda}_r}^{\boldsymbol{\lambda}_v}(t, t_0) & \boldsymbol{\Phi}_{\boldsymbol{\lambda}_v}^{\boldsymbol{\lambda}_v}(t, t_0) \end{bmatrix} \delta\mathbf{y}_0 \tag{13}$$

Substituting in to the cost function, we then have

$$J = \frac{1}{2}\delta\mathbf{y}_0^T \left(\int_{t_0}^{t_f} \left(\boldsymbol{\Phi}_{\mathbf{y}}^{\boldsymbol{\lambda}_v}(t, t_0) \right)^T \left(\boldsymbol{\Phi}_{\mathbf{y}}^{\boldsymbol{\lambda}_v}(t, t_0) \right) dt \right) \delta\mathbf{y}_0 \tag{14}$$

With the linearized analysis, we explicitly solve for the initial costates that satisfy the linearized boundary value problem constraints

$$\delta\boldsymbol{\lambda}_0 = \begin{bmatrix} -\left(\boldsymbol{\Phi}_{\boldsymbol{\lambda}}^{\mathbf{x}}\right)^{-1} \boldsymbol{\Phi}_{\mathbf{x}}^{\mathbf{x}} & \left(\boldsymbol{\Phi}_{\boldsymbol{\lambda}}^{\mathbf{x}}\right)^{-1} \end{bmatrix} \begin{bmatrix} \delta\mathbf{x}_0 \\ \delta\mathbf{x}_f \end{bmatrix} \tag{15}$$

which then can be used to find the full, initial, augmented state in terms of the boundary conditions

$$\delta\mathbf{y}_0 = \begin{bmatrix} \mathbf{I}_6 & \mathbf{0}_6 \\ -\left(\boldsymbol{\Phi}_{\boldsymbol{\lambda}}^{\mathbf{x}}\right)^{-1} \boldsymbol{\Phi}_{\mathbf{x}}^{\mathbf{x}} & \left(\boldsymbol{\Phi}_{\boldsymbol{\lambda}}^{\mathbf{x}}\right)^{-1} \end{bmatrix} \begin{bmatrix} \delta\mathbf{x}_0 \\ \delta\mathbf{x}_f \end{bmatrix} \tag{16}$$

We define the matrix

$$\mathbf{E} = \begin{bmatrix} \mathbf{I}_6 & \mathbf{0}_6 \\ -\left(\mathbf{\Phi}^{\mathbf{x}}_{\boldsymbol{\lambda}}\right)^{-1}\mathbf{\Phi}^{\mathbf{x}}_{\mathbf{x}} & \left(\mathbf{\Phi}^{\mathbf{x}}_{\boldsymbol{\lambda}}\right)^{-1} \end{bmatrix}^T \int_{t_0}^{t_f} \left(\mathbf{\Phi}^{\boldsymbol{\lambda}_v}_{\mathbf{y}}(t,t_0)\right)^T \left(\mathbf{\Phi}^{\boldsymbol{\lambda}_v}_{\mathbf{y}}(t,t_0)\right) dt \begin{bmatrix} \mathbf{I}_6 & \mathbf{0}_6 \\ -\left(\mathbf{\Phi}^{\mathbf{x}}_{\boldsymbol{\lambda}}\right)^{-1}\mathbf{\Phi}^{\mathbf{x}}_{\mathbf{x}} & \left(\mathbf{\Phi}^{\mathbf{x}}_{\boldsymbol{\lambda}}\right)^{-1} \end{bmatrix} \tag{17}$$

which can be used to determine the energy-constrained reachable set for our system.[13,14] Substituting in to the cost function, we now have

$$J = \frac{1}{2}\begin{bmatrix}\delta\mathbf{x}_0 \\ \delta\mathbf{x}_f\end{bmatrix}^T \mathbf{E} \begin{bmatrix}\delta\mathbf{x}_0 \\ \delta\mathbf{x}_f\end{bmatrix} \tag{18}$$

Relative reachable set theory considers the set of $\delta\mathbf{x}_f$ that can be reached given some fixed starting condition $\delta\mathbf{x}_0$ or some set of potential starting points $\delta\mathbf{x}_0$. Much of this energy-limited reachable set theory is accomplished using ellipsoidal geometry associated with the quadratic form described by the matrix $\mathbf{E}$ and the eigenvalue decomposition. We will use these same techniques as well as extensions to generalized eigenvalues and eigenvectors to study the set of state-return trajectories that satisfy an energy constraint.

State-returning trajectories in the vicinity of a periodic reference orbit satisfy the condition $\delta\mathbf{x}_f = \delta\mathbf{x}_0$, so that the final state is equivalent to the initial state after one period of the reference periodic orbit. To study the set of state-return trajectories that require less than some energy limit, we may study the following matrix

$$\mathbf{E}^* = \begin{bmatrix}\mathbf{I}_6 & \mathbf{I}_6\end{bmatrix} \mathbf{E} \begin{bmatrix}\mathbf{I}_6 & \mathbf{I}_6\end{bmatrix}^T \tag{19}$$

so that the linearized cost function for the state-return trajectory beginning and ending at $\delta\mathbf{x}_0$ can then be written as

$$J = \frac{1}{2}\delta\mathbf{x}_0^T\mathbf{E}^*\delta\mathbf{x}_0 \tag{20}$$

Now assume that $(\gamma_i, \mathbf{w}_i)$ is an eigenpair of the matrix $\mathbf{E}^*$ where γ_i is some eigenvalue and $\mathbf{w}_i$ is its corresponding eigenvector. Since $\mathbf{E}^*$ is a symmetric positive semi-definite matrix, the set of possible relative states $\delta\mathbf{x}_0$ that cost less than some energy limit J^* to begin and end at under linearized optimal control is given by the hyper-ellipsoid described by the set

$$\left\{\delta\mathbf{x}_0 \quad \text{s.t.} \quad \frac{1}{2}\delta\mathbf{x}_0^T\mathbf{E}^*\delta\mathbf{x}_0 \leq J^*\right\} \tag{21}$$

whose semi-axes are given by the vectors

$$\mathbf{a}_i = \sqrt{\frac{2J^*}{\gamma_i}}\mathbf{w}_i \tag{22}$$

Thus, we have defined the set of relative states which can be returned to in a period of the reference orbit with cost no greater than J^*. The ellipsoid described here is in 6-dimensional position and velocity space.

INVESTIGATION AND ANALYSIS

Our initial investigation involves selecting a reference halo orbit around L2. Because the reference orbit is naturally periodic, the initial phasing may be chosen at will. Here, we select the initial

condition at apolune. The initial conditions for our chosen orbit are

$$\begin{bmatrix} x \\ y \\ z \\ v_x \\ v_y \\ v_z \\ \boldsymbol{\lambda} \end{bmatrix} = \begin{bmatrix} 1.06315768 \text{ DU} \\ 0.000326952322 \text{ DU} \\ -0.200259761 \text{ DU} \\ 0.000361619362 \text{ DU/TU} \\ -0.176727245 \text{ DU/TU} \\ -0.000739327422 \text{ DU/TU} \\ \mathbf{0}_{6\times 1} \end{bmatrix} \tag{23}$$

with a period of 2.085034838884136 TU and a mass constant of 0.01215059.

Propagation of our states and STMs is performed numerically in canonical units with an explicit 8th order Runge-Kutta integrator with absolute and relative error tolerances set to 1e-13. All computation is handled through precomputed STMs for the reference trajectory, as used in previous studies.[15]

Validation

In order to validate our method, we use a Newton-Raphson iteration scheme to find the true energy-optimal cost of our target orbits. We first determine the "inherent cost" to maintain the periodic reference orbits that we select. Although in theory these naturally periodic orbits should require no cost to maintain, there is typically some inherent numerical error in the initial conditions. Thus, the "true" cost includes error from the imperfect initial conditions. This is important for the validation analysis because the cost found by the Newton-Raphson scheme is inaccurate for cases where the cost would be lower or near the orbit's inherent cost. Therefore, we only consider the costs of orbits that are at least an order of magnitude greater than this inherent cost. Our reference trajectory's inherent cost is $\approx$ 3.5e-14 DU^2/TU^3.

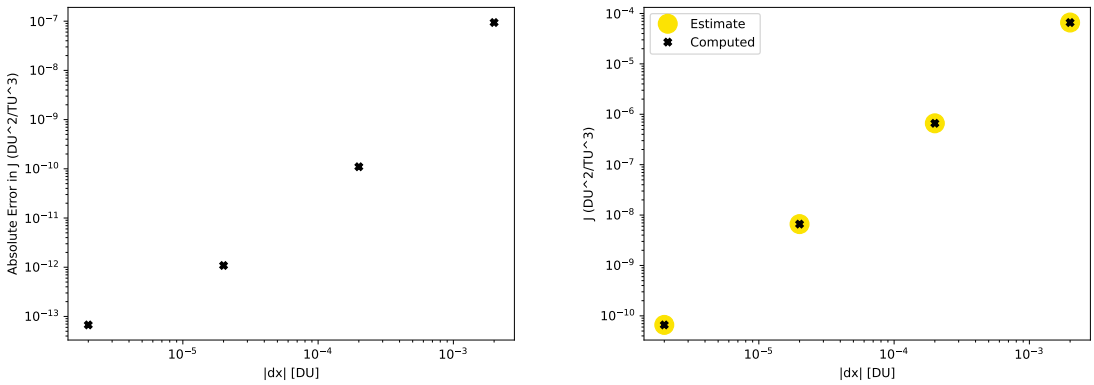

Figure 1: The difference between the estimated and computed costs (left) and the estimated and computed costs (right).

In Figure 1, we see that the cost to maintain a periodic orbit follows a quadratic form and that the linear analysis provides a good approximation of the full nonlinear analysis. In the range of Figure 1, the error is at least 3 orders of magnitude below the true cost value (corresponding to $< 0.1\%$

error). The error grows as $\delta\mathbf{x}_0$ increases, as expected in this analysis. For deviations less than that shown in Figure 1, the linear analysis should be a good approximation of the true cost, although the inherent cost does begin to dominate the error.

Addition of Thrust Constraint

We now introduce a thrust constraint to analyze the extents of the energy-limited reachable set. For a given spacecraft with maximum acceleration from thrust $u_{\max}$ and with the assumption that the spacecraft will thrust for the entire orbital period, we can find

$$J^* = \frac{1}{2}u_{\max}^2(t_f - t_0) \tag{24}$$

where $t_f - t_0$ is the time required to complete a single period. As it is written, J^* may be understood as the maximum specific power expended during a single orbit. With this constraint, we can solve for the extents of the semiaxes of the energy-limited reachable set. For a base design, let us assume a representative spacecraft with an initial mass of 1000 kg and thrust of 50 mN, translating to $u_{\max}$ = 5E-5 m/s^2 $\approx$ 0.0184 DU/TU^2 and J^* = 3.51E-4 DU^2/TU^3. This cost constraint is selected, in particular, because it falls in the range of costs with $< 1\%$ error and is a currently achievable thrust level for a propulsion system. Thus, it makes for a good example of this analysis.

Table 1: The extents and corresponding directions of the semiaxes for the cost, J^* = 3.51E-4 DU^2/TU^3. The directions are given by the eigenvectors of $\mathbf{E}^*$. The extents are listed from largest to smallest, corresponding to least expensive to most expensive directions to deviate from the reference in.

Extent [DU]	Direction [DU, DU, DU, DU/TU, DU/TU, DU/TU]
15918.250	[0.00075547 -0.36919333 -0.00154457 -0.40833012 -0.00219097 0.83483833]
0.01984495	[-0.4073362 -0.00359944 -0.29024187 -0.00429968 0.86591161 -0.00159068]
0.00892213	[0.00166912 -0.0949137 0.00474959 -0.87702446 -0.00323734 -0.47093912]
0.00460856	[0.58703528 -0.00312857 0.64311054 0.00223334 0.4917122 0.00165787]
0.00244912	[0.69940335 0.02398051 -0.70835806 -0.00809316 0.09164505 0.00494355]
0.00051309	[-0.01727422 0.92416983 0.01929803 -0.25299333 0.00145136 0.28501156]

Using the thrust constraint paired with the linear analysis, we can study the reachable set. The reachable set takes the shape of a 6-dimensional hyper-ellipsoid with extents and semi-axes directions specified by the thrust constraint and eigenstructure of $\mathbf{E}^*$, as listed in Table 1. The directions of the semi-axes are given by the eigenvectors of $\mathbf{E}^*$ and the extents of the semi-axes can be found by taking the magnitude of Equation 22. The eigenvector associated with the smallest eigenvalue corresponds to the least expensive direction to deviate from the reference trajectory, which presents itself as the largest semi-axis extent. In this case, the largest extent should be infinite, as it corresponds to the zero eigenvalue. However, there is numerical error and so the first eigenvalue has a finite length here. For this reason, we do not present results that correspond to deviations in the direction of the first eigenvector.

Figure 2 shows the physical extents in position space of the trajectories. We sample from the boundaries of the six-dimensional reachable set 100,000 times and solve the linearized boundary value problem for each set of initial deviations to obtain initial costates. We then linearly propagate

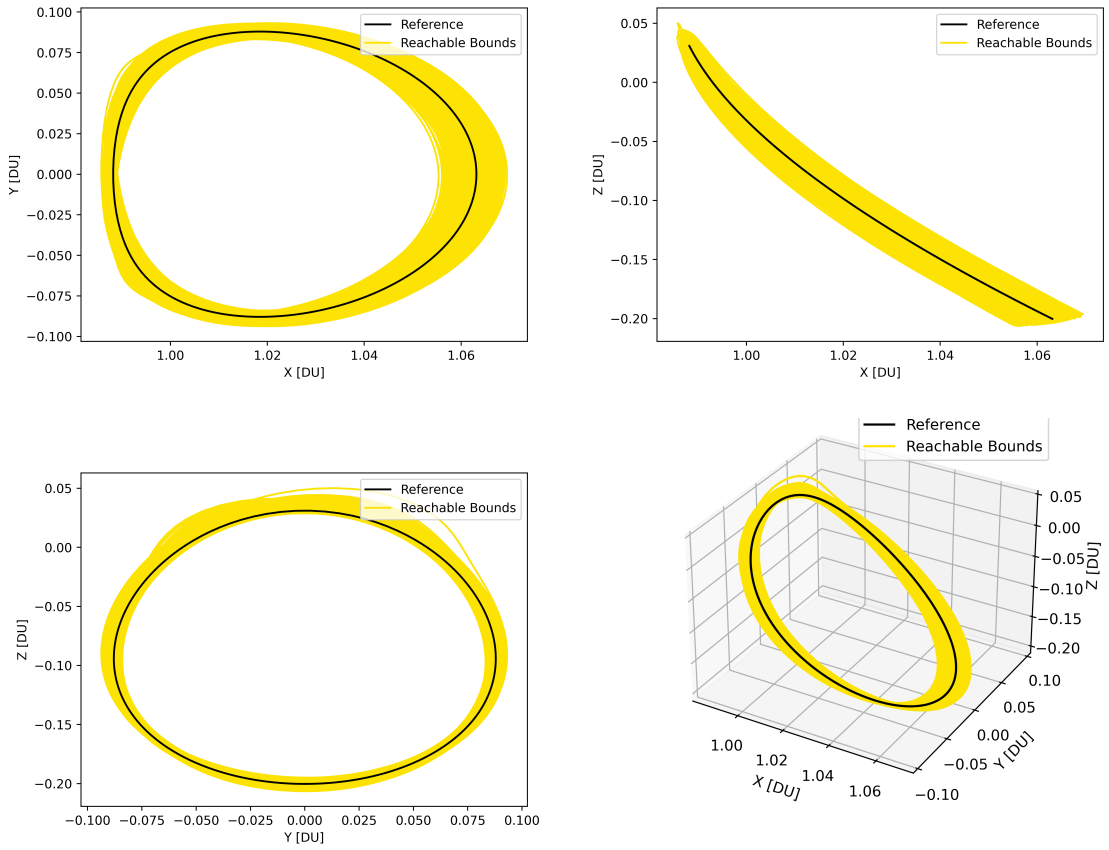

Figure 2: The reachable sets in position space via sampling with J^* = 3.51E-4 DU^2/TU^3.

the augmented state deviations and costates and plot all the resulting trajectories in some lower-dimensional space. Due to the constraints of sampling, the reachable bounds in Figure 2 are not solid and display some gaps and asymmetries. These are products of incomplete sampling and the true reachable set does not display these phenomena. In Figure 2, the greatest deviation in the x direction is found at apolune, where the orbit is initialized. This can also be seen in Figure 3, where deviations in the x and z directions are maximized when at apolune. Likewise, the smallest deviations are found at perilune, our half-period. The size of the bounded region is a function of J^*, as increasing the cost will expand the reachable set.

Notice in Figure 3 that the orbits begin and conclude at the same point, as expected of periodic trajectories. However, the costates and thus the thrust do not necessarily begin and end at the same values. Thus, the augmented state is not necessarily periodic but the state that strictly includes the position and velocity vectors is periodic. Figure 3 is particularly insightful in how deviations in the initial condition can cascade through the orbit. For example, assume we wish to decrease perilune distance for our spacecraft in order to obtain better images of the Lunar surface. In order to achieve this, the spacecraft should deviate such that $\delta x < 0$, $\delta z < 0$, and $\delta y = 0$ at perilune. From inspection of Figure 3, deviations along the direction of the fifth eigenvector will achieve this, as it fulfills these three qualities. The fifth eigenvector corresponds to the second most-expensive

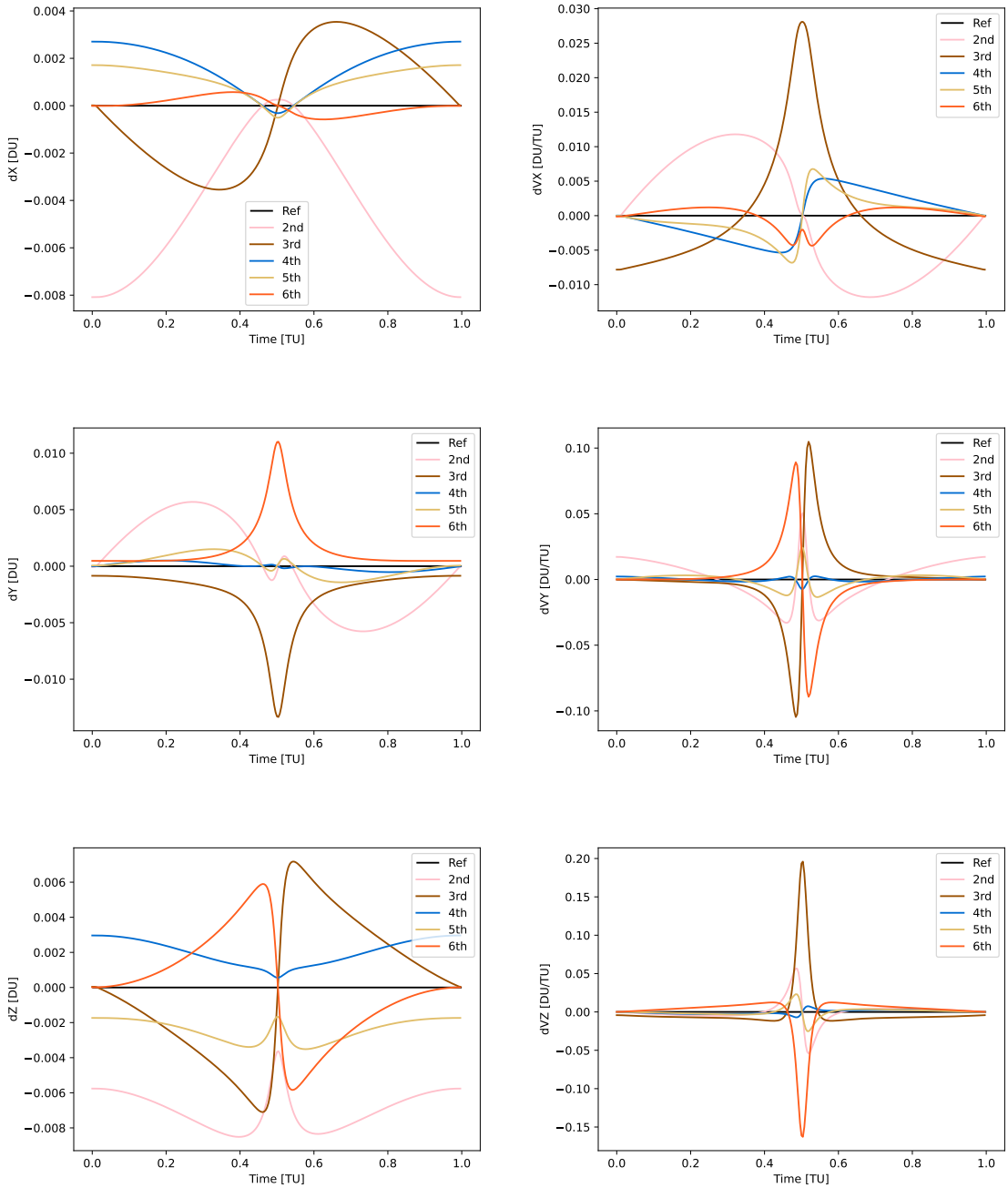

Figure 3: The difference between the reference trajectory and deviations in the final five eigenvectors.

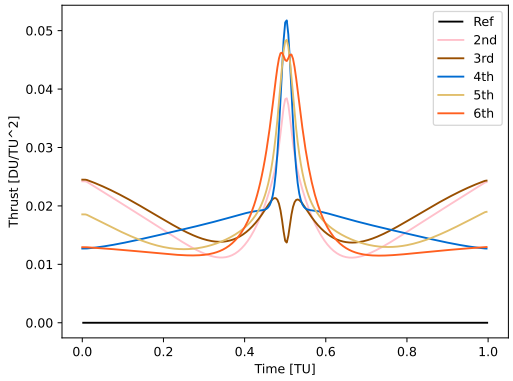

Figure 4: The thrusting magnitude over a single orbit for deviations in the final five eigenvectors.

direction to deviate from the reference, so this also indicates that reduction in perilune distance is relatively expensive.

CONCLUSIONS

With this analysis, we have specified bounds on forced periodic structures in the CR3BP. These structures are likely to provide unique observation and operational opportunities for satellites. We analyzed these forced periodic structures via linear analysis and we determine that for the energy-optimal case, the full augmented state is not periodic but the state that only includes position and velocity is periodic. The linear analysis also allows us to determine the least and most costly directions that deviations to the state may be made. In particular, deviations along the fifth eigenvector listed in Table 1, corresponding to the second-largest eigenvalue, will reduce the perilune distance of a spacecraft for our reference orbit.

ACKNOWLEDGEMENTS

The authors would like to thank Robin Amstrong for helpful discussions on subspace perturbation theory and Jackson Shannon for insightful recommendations. Jackson Kulik would like to thank the DOD National Defense Science and Engineering Graduate Fellowship for support. This material is based upon work supported by the Air Force Office of Scientific Research under award number FA9550-23-1-0665.

APPENDIX

2D Projections of Hyper-Ellipsoids Describing the Energy-Constrained Reachable Set

This paper develops a mathematical description of the reachable set of states relative to a reference trajectory. The ellipses in Figure 5 are 2-dimensional projections of 6-dimensional hyper-ellipsoids calculated for various states along the reference trajectory. These hyper-ellipsoids describe the energy-constrained reachable set of forced periodic trajectories. The matrix $\mathbf{E}$ from Eq. 17 can be utilized to determine the energy-constrained reachable set of the system. This matrix is then used to produce $\mathbf{E}^*$, as shown in Eq. 19. The first step needed to generate a 2-dimensional projection of the reachable set is to solve the eigenvalue problem in Eq. 25.

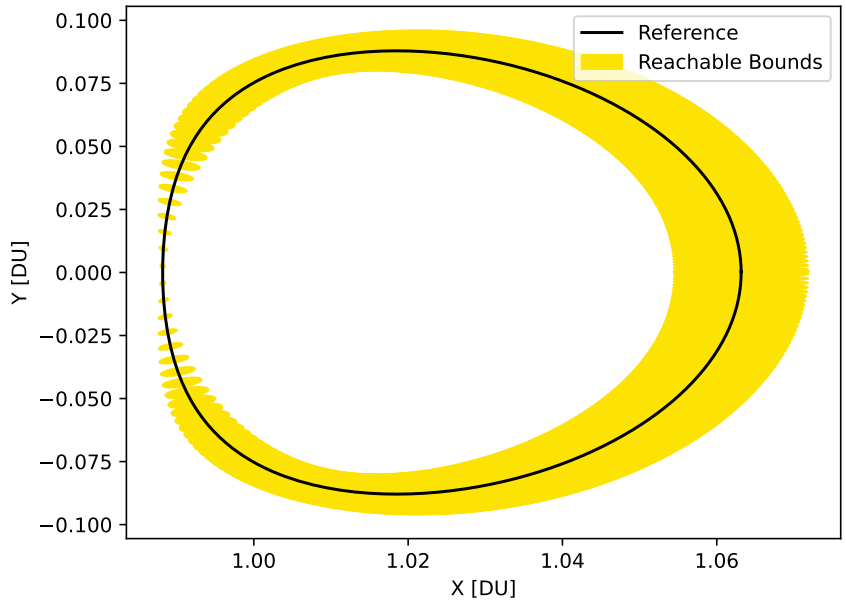

Figure 5: Sample of XY-plane projections of hyper-ellipsoids along a reference trajectory

$$\mathbf{E}^{*}\mathbf{w} = \gamma\mathbf{w} \tag{25}$$

A diagonal matrix of eigenvalues of $\mathbf{E}^{*}$ can be written as

$$\mathbf{\Gamma} = \begin{bmatrix} \gamma_1 & 0 & 0 & 0 & 0 & 0 \\ 0 & \gamma_2 & 0 & 0 & 0 & 0 \\ 0 & 0 & \gamma_3 & 0 & 0 & 0 \\ 0 & 0 & 0 & \gamma_4 & 0 & 0 \\ 0 & 0 & 0 & 0 & \gamma_5 & 0 \\ 0 & 0 & 0 & 0 & 0 & \gamma_6 \end{bmatrix}. \tag{26}$$

with eigenvalues listed in ascending order. A 6x6 matrix of eigenvectors corresponding to the eigenvalues is written as

$$\mathbf{W} = \begin{bmatrix} \mathbf{w}_1 & \mathbf{w}_2 & \mathbf{w}_3 & \mathbf{w}_4 & \mathbf{w}_5 & \mathbf{w}_6 \end{bmatrix}. \tag{27}$$

The actual values in these matrices are calculated for the reference trajectory in Figure 5 using the eigh function in the linalg submodule of Python's NumPy library.[16] γ_1 and $\mathbf{w}_1$ are the eigenvalue and eigenvector associated with the hyper-ellipsoid's axis of infinite extent. They must be removed from their respective matrices in order to develop projections like those seen in Figure 5. Removing them leads to a new 5x5 diagonal matrix of eigenvalues

$$\mathbf{\Gamma}' = \begin{bmatrix} \gamma_2 & 0 & 0 & 0 & 0 \\ 0 & \gamma_3 & 0 & 0 & 0 \\ 0 & 0 & \gamma_4 & 0 & 0 \\ 0 & 0 & 0 & \gamma_5 & 0 \\ 0 & 0 & 0 & 0 & \gamma_6 \end{bmatrix}. \tag{28}$$

and 6x5 matrix of remaining eigenvectors

$$\mathbf{W}' = \begin{bmatrix} \mathbf{w}_2 & \mathbf{w}_3 & \mathbf{w}_4 & \mathbf{w}_5 & \mathbf{w}_6 \end{bmatrix}. \tag{29}$$

Once the eigenvector and eigenvalue matrices are modified to disregard the axis of infinite extent, a second eigenvector problem is formulated to determine the characteristics of the ellipse representing the projection of the 6D hyper-ellipsoid onto 2D space. A 2-dimensional projection requires a 2x6 matrix $\mathbf{A}$ that specifies the desired projection space. Each of the six columns of $\mathbf{A}$ is associated with a corresponding entry of the state vector $\mathbf{x}$. For example, a matrix specifying a projection onto the XY-plane is written as

$$\mathbf{A}_{x,y} = \begin{bmatrix} 1 & 0 & 0 & 0 & 0 & 0 \\ 0 & 1 & 0 & 0 & 0 & 0 \end{bmatrix}. \tag{30}$$

A new eigenvector problem incorporating the projection matrix $\mathbf{A}$ is formulated as

$$\mathbf{W'^T A^T A W' z} = \lambda \mathbf{\Gamma' z} \tag{31}$$

The eigenvalues and eigenvectors that satisfy the above equation are described by the diagonal matrix of ascending eigenvalues

$$\begin{bmatrix} \lambda_1 & 0 & 0 & 0 & 0 \\ 0 & \lambda_2 & 0 & 0 & 0 \\ 0 & 0 & \lambda_3 & 0 & 0 \\ 0 & 0 & 0 & \lambda_4 & 0 \\ 0 & 0 & 0 & 0 & \lambda_5 \end{bmatrix} \tag{32}$$

with corresponding eigenvectors

$$\begin{bmatrix} \mathbf{z}_1 & \mathbf{z}_2 & \mathbf{z}_3 & \mathbf{z}_4 & \mathbf{z}_5 \end{bmatrix} \tag{33}$$

Information needed to describe the directions of the semi-axes of the projection are stored in $\mathbf{z_4}$ and $\mathbf{z_5}$. The eigenvector associated with the small extent $\mathbf{z}_b$ and the eigenvector associated with the large extent $\mathbf{z}_a$ are

$$\mathbf{z}_b = \mathbf{z}_4 \tag{34}$$

$$\mathbf{z}_a = \mathbf{z}_5 \tag{35}$$

These vectors are then normalized using

$$\hat{\mathbf{z}}_a = \frac{\mathbf{z}_a}{\|\mathbf{z}_a\|} \tag{36}$$

$$\hat{\mathbf{z}}_b = \frac{\mathbf{z}_b}{\|\mathbf{z}_b\|} \tag{37}$$

In the 2D projection space, the direction of the larger semi-axis of the projected-energy ellipsoid is specified by the 2x1 unit vector

$$\hat{\mathbf{a}} = \mathbf{A}\mathbf{W}'\mathbf{z}_a \tag{38}$$

The direction of the smaller semi-axis is specified by the 2x1 unit vector

$$\hat{\mathbf{b}} = \mathbf{A}\mathbf{W}'\mathbf{z}_b \tag{39}$$

The energy limit J^* included in the cost function of the optimal control is reintroduced to obtain the lengths of the ellipse's semi-axes. The semi-axis length a is given by

$$a = \sqrt{2J^*\lambda_5} \tag{40}$$

and the semi-axis length b is given by

$$b = \sqrt{2J^*\lambda_4} \tag{41}$$

Lastly, the center-coordinates of the ellipse are equal to the center-coordinates of the 6-dimensional hyper-ellipsoid that are associated with the projection space. Using the process above, all the characteristics needed to describe a 2D projection of a 6D hyper-ellipsoid are determined. These characteristics are the ellipse's center-coordinates, lengths of semi-axes, and directions of semi-axes.

One ellipse representing the projection of a single hyper-ellipsoid does not capture the energy-constrained reachable set of orbits along the entire reference trajectory in a single image. Every state along the reference trajectory is associated with its own 6D hyper-ellipsoid describing the set of reachable forced periodic trajectories relative to that state. Figure 5 displays 2D projections for a sample of 260 states, each corresponding to its own ellipse. To obtain these ellipses, the cocycle conditions for state transition matrices and state transition tensors (STTs) were utilized to calculate a full-period STM and STT for each sampled point along the reference trajectory. As shown in Eq. 17, the state-transition matrices used to calculate $\mathbf{E}$ correspond to a full period. Starting from time t_0 = 0, STMs for the reference trajectory are precomputed and used to propagate the initial state specified in Eq. 23. These STMs can be stored in a 3-dimensional array such that each layer of the array stores an STM $\mathbf{\Phi}(t_i, t_0)$ associated with a time t_i at index i and an initial time t_0. To generate a hyper-ellipsoid centered at the initial conditions in Eq. 23, the full period STM $\mathbf{\Phi}(t_f, t_0)$ is inserted into the matrix $\mathbf{E}$. Projecting this hyper-ellipsoid into 2D space results in an ellipse with center-coordinates corresponding to the relevant initial conditions in the state vector. For example, the first ellipse created in the XY projection in Figure 5 is centered at (1.06315768 DU, 0.000326952322 DU).

Cocycle conditions are introduced to obtain the other full-period STMs and STTs for the sampled points along the reference trajectory. The semigroup property of STMs is written as

$$\mathbf{\Phi}(t_2, t_0) = \mathbf{\Phi}(t_2, t_1)\mathbf{\Phi}(t_1, t_0) \tag{42}$$

As previously stated, the STMs utilized to create the projections in Figure 5 are stored in a 260-layer array. Using this array and the semigroup property above, a full period STM associated with the state at a sampled time t_i in the reference trajectory is described by

$$\mathbf{\Phi}(t_i, t_i - (t_f - t_0)) = \mathbf{\Phi}(t_i, t_0)\mathbf{\Phi}(t_f, t_0)\mathbf{\Phi}^{-1}(t_i, t_0) \tag{43}$$

For notational purposes, the above full-period STM can be written as

$$\mathbf{\Phi}_i = \mathbf{\Phi}(t_i, t_i - (t_f - t_0)) \tag{44}$$

with t_f representing the time associated with the last index of the 3D array that stores STMs propagated from t_0. The above equation reflects that the trajectory of the spacecraft is periodic. The position-velocity state at the first time-index of the orbital period matches the state at the final time-index of the orbital period. Similar to the STMs, the STTs associated with propagating the initial conditions from Eq. 23 can also be stored in a 3D array. A full-period STT asscociated with a given index i in the array is written as

$$\begin{aligned}\mathbf{\Psi}_i = &\big(\mathbf{\Phi}(t_f, t_0)\mathbf{\Phi}^{-1}(t_i, t_0)\big)^T \mathbf{\Psi}(t_i, t_0)\big(\mathbf{\Phi}(t_f, t_0)\mathbf{\Phi}^{-1}(t_i, t_0)\big) \\ &+ (\mathbf{\Phi}(t_i, t_0)^T)^{-1}\big(\mathbf{\Psi}(t_f, t_0) - \mathbf{\Psi}(t_i, t_0)\big)\mathbf{\Phi}^{-1}(t_i, t_0).\end{aligned} \tag{45}$$

with $\mathbf{\Psi}_i$ following the same notational standard as $\mathbf{\Phi}_i$ in Eq. 44.

From any given $\mathbf{\Psi}_i$ in the array, a matrix $\mathbf{E}_i$ that is used to describe a hyper-ellipsoid centered at a particular state along the reference trajectory can be formed. $\mathbf{E}_i$ is constructed as

$$\mathbf{E}_i = \begin{bmatrix} \mathbf{I}_6 & \mathbf{0}_6 \\ -\left(\mathbf{\Phi}^{\mathbf{x}}_{\boldsymbol{\lambda},i}\right)^{-1}\mathbf{\Phi}^{\mathbf{x}}_{\mathbf{x},i} & \left(\mathbf{\Phi}^{\mathbf{x}}_{\boldsymbol{\lambda},i}\right)^{-1} \end{bmatrix}^T \mathbf{\Psi}_i \begin{bmatrix} \mathbf{I}_6 & \mathbf{0}_6 \\ -\left(\mathbf{\Phi}^{\mathbf{x}}_{\boldsymbol{\lambda},i}\right)^{-1}\mathbf{\Phi}^{\mathbf{x}}_{\mathbf{x},i} & \left(\mathbf{\Phi}^{\mathbf{x}}_{\boldsymbol{\lambda},i}\right)^{-1} \end{bmatrix} \tag{46}$$

Using the above equations, it is possible to construct the $\mathbf{E}$ matrix for any point along the reference orbit using only the STMs and STTs propagated for the initial conditions in Eq. 23. Increasing the sample size of points used to produce Figure 5 to an infinitely large number of points along the reference trajectory would result in an image that fully captures the energy-constrained reachable set for the entire reference trajectory. This would eliminate visible gaps between ellipses on the perilune-side of the orbit (the left side of the XY projection). Generating STMs and STTs for a large number of points along the reference trajectory is computationally costly, so a cubic spline interpolation method is utilized to fill in the gaps between ellipses seen in Figure 5. This method generates more ellipses between sampled points based on the center-coordinates, semi-axes lengths, and rotation angles of nearby ellipses, resulting in the projections in Figure 6.

Tangent Line Method for Specifying Reachable Set in Projection Space

After projecting a set of hyper-ellipsoids into 2D space using the method in the previous section, it is possible to specify the boundaries of the reachable set using tangent lines between consecutive ellipses. An ellipse is described by the coordinates of its center (h, k), its semi-axes a and b, and the rotation angle r between its long semi-axis and the horizontal axis of the projection space. For every set of two overlapping ellipses, there are two lines that are tangent to both ellipses. These lines are determined by solving the system specified in Eq. 47 for $p_1, p_2, x_1, x_2, y_1, y_2$, and m.

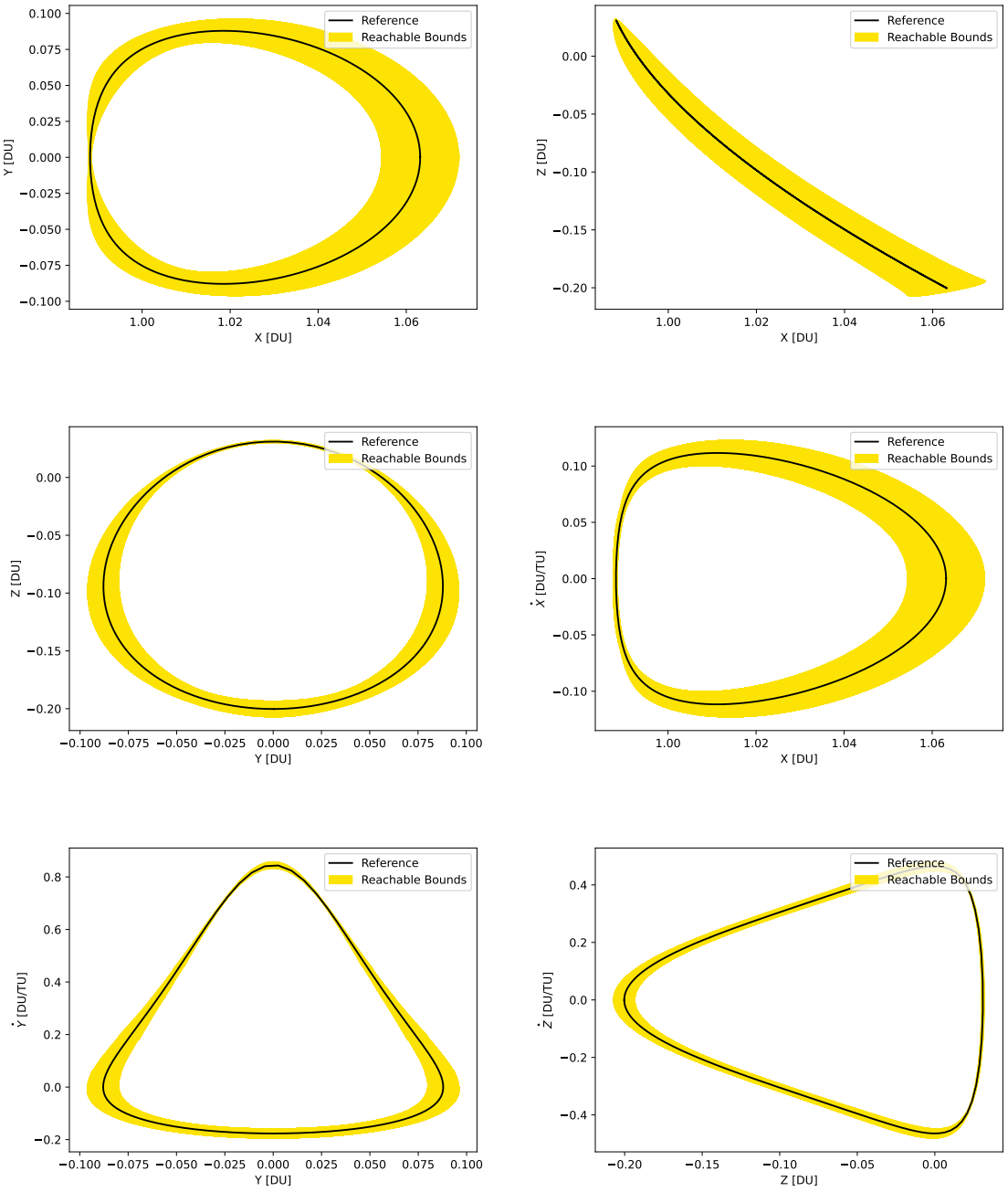

Figure 6: The reachable sets via sampling and interpolation with J^* = 3.51E-4 DU^2/TU^3.

$$\begin{cases} x_1 = (h_1 + a_1\cos(p_1)\cos(r_1) - b_1\sin(p_1)\sin(r_1)) \\ y_1 = (k_1 + a_1\cos(p_1)\sin(r_1) + b_1\sin(p_1)\cos(r_1)) \\ x_2 = (h_2 + a_2\cos(p_2)\cos(r_2) - b_2\sin(p_2)\sin(r_2)) \\ y_2 = (k_2 + a_2\cos(p_2)\sin(r_2) + b_2\sin(p_2)\cos(r_2)) \\ m = \frac{(y_2 - y_1)}{(x_2 - x_1)} \\ m = \frac{\left(-\frac{b_1}{a_1}\cot(p_1) + \tan(r_1)\right)}{\left(1 + \frac{b_1}{a_1}\cot(p_1)\tan(r_1)\right)} \\ m = \frac{\left(-\frac{b_2}{a_2}\cot(p_2) + \tan(r_2)\right)}{\left(1 + \frac{b_2}{a_2}\cot(p_2)\tan(r_2)\right)} \end{cases} \tag{47}$$

(x_1, y_1) and (x_2, y_2) are the coordinates in the projection-space where the tangent line collides with the first and second ellipse, respectively. p_1 and p_2 are angles used in the parametric equation for an ellipse that correspond to (x_1, y_1) and (x_2, y_2).[17] Lastly, m is the slope of the tangent line.

The above set of nonlinear equations can be solved using an optimizer. The tangent lines in Figure 7 are determined using the minimize function in Python's scipy.otpimize module. The optimization algorithm used to produce the figure is the Sequential Least Squares Programming algorithm (SLSQP).[18] Seven constraints matching the above equations and a trivial objective function were introduced to solve for each tangent line. The seemingly continuous boundary lines in Figure 7 actually consist of many independent tangent lines determined from solving 518 nonlinear optimization problems. Reasonable initial guesses and solution boundaries for each problem are critical for the optimizer to converge to a solution all 518 times. Even if these conditions are reasonable, it is often difficult for the optimizer to converge to a solution, particularly in areas where tangent lines have high slopes (such as the left side of the XY projection in Figure 7). To aid the optimizer in these areas, it is useful to rotate the pair of ellipses that form the system of equations so that the optimizer solution will have a low slope. To accomplish this for a particular set of ellipses, the angle of the line connecting ellipses' centers relative to the horizontal axis is determined using the equation below.

$$\phi = \arctan\frac{k_2 - k_1}{h_2 - h_1} \tag{48}$$

It is reasonable to assume the tangent line to both ellipses will have a slope similar to the slope of the line connecting ellipses' centers. For this reason, it is useful to rotate each ellipse so that the slope of the line connecting their centers is zero. This is achieved by rotating the center coordinates of each ellipse and modifying each rotation angle according to the following equations:

$$\begin{bmatrix} h' \\ k' \end{bmatrix} = \begin{bmatrix} \cos\phi & \sin\phi \\ -\sin\phi & \cos\phi \end{bmatrix} \begin{bmatrix} h \\ k \end{bmatrix} \tag{49}$$

$$r' = r - \phi \tag{50}$$

The new variables h', k', and r' can then be utilized in place of the original variables in the nonlinear system of equations describing a tangent line to both ellipses. The unknown variables in

the rotated version of the problem are referred to as $p_1', p_2', x_1', x_2', y_1', y_2'$, and m'. Once a solution is obtained, (x_1', y_1') and (x_2', y_2') can be rotated using the transpose of the rotation matrix in Eq. 49 to achieve the original desired solutions (x_1, y_1) and (x_2, y_2). These coordinates can then be used to determine p_1, p_2, and m. The process for rotating each set of ellipses significantly increased the number of solutions found for each set of projections. Before the rotation method was implemented, the optimizer only determined 476 of 518 tangent lines in the XY projection shown in Figure 7. After applying rotations in cases where the optimizer failed to solve the unmodified system of equations, all 518 solutions were found. All 518 solutions in the YZ projection in Figure 7 were also found after implementing the rotation method.

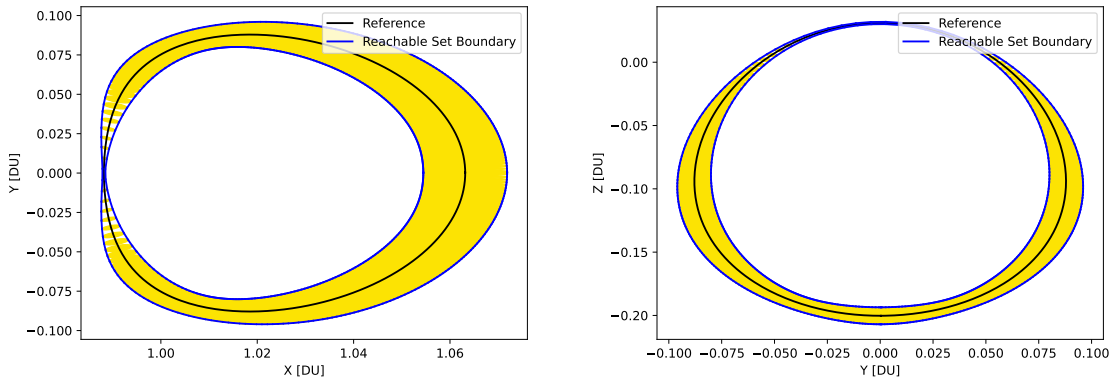

Figure 7: Boundaries of reachable set projection with J^* = 3.51E-4 DU^2/TU^3 determined using tangent line method.

TEXT FOR JOURNAL

We compare the first through fourth semi-axes to the center eigenspace of the monodromy matrix. We find that the direction of the first semi-axis is consistent with the along-track direction of the monodromy matrix. In fact, we find that they are only separated by an angle of $\theta \approx 0.00004^\circ$. The second semi-axis is relatively similar to the direction that corresponds to the orbit families with an angle of $\theta \approx 4.607^\circ$. However, the third and fourth semi-axes do not tend to correspond to directions defined by the center eigenspace of the monodromy matrix. However, the third eigenvector is $\theta \approx 48.992^\circ$ from the closest portion of the center eigenspace whereas the fourth eigenvector is $\theta \approx 81.653^\circ$ from the center eigenspace. We find that for more costly deviations to the reference trajectory, there is less consistency with the center eigenspace of the monodromy matrix.

Analyzing the Subspace of Least Expensive forced periodic structures

We conjecture that state deviations within the center eigenspace of the uncontrolled periodic reference trajectory will be likely to exhibit lower costs when control is employed to achieve a forced periodic structure beginning and ending at that deviation as compared with deviations that have components lying in the stable or unstable eigenspaces. This is reasonable to expect because state deviations in the stable and unstable eigenspaces will have a tendency to shrink or grow exponentially, respectively, in time in a manner that control will need to counteract to return to the same state at a later time. Thus, deviations into the stable and unstable eigenspaces should necessarily be

more expensive rather than deviations of the same magnitude within the center eigenspace of the reference trajectory.

In order to validate this conjecture we may employ principal/canonical angle analysis on subspaces.[19,20] Here, we introduce the monodromy matrix, which is the matrix that results from propagating $\mathbf{\Phi}_{\mathbf{x}}^{\mathbf{x}}$ for a single period. We then compare the four-dimensional center eigenspace of the monodromy matrix and the space spanned by the four eigenvectors of $\mathbf{E}^*$ associated with the four smallest eigenvalues (and thus the lowest cost forced periodic structures). Let $\mathbf{W} \in \mathbb{R}^{6,4}$ be the matrix whose columns are given my the eigenvectors $\mathbf{w}_i$ associated with the smallest eigenvalues of $\mathbf{E}^*$. Given that $\mathbf{E}^*$ is a symmetric positive definite matrix, the columns of $\mathbf{W}$ are mutually orthogonal. Let $\mathbf{C} \in \mathbb{R}^{6,4}$ consist of an orthogonal column basis of the center eigenspace of the monodromy matrix associated with the reference periodic orbit. The center eigenspace of the monodromy matrix is given by taking the two pairs of complex conjugate eigenvectors $\mathbf{c}_{i_1} = \bar{\mathbf{c}}_{i_2}$ associated with unit modulus eigenvalues of the monodromy matrix and constructing the span of the following real vectors: $\mathbf{c}_{i_1} + \mathbf{c}_{i_2}$ (the real part of both eigenvectors) and $i(\mathbf{c}_{i_1} - \mathbf{c}_{i_2})$ (the imaginary part of both eigenvectors). Given these four real vectors spanning the center eigenspace that are not necessarily unit normed or orthogonal, we can construct $\mathbf{C}$ with orthonormal columns that form a basis for the center eigenspace by taking $\mathbf{C}$ equal to the matrix $\mathbf{Q}$ from the skinny QR decomposition of the matrix with columns given by the four not necessarily orthogonal or unit-normed real vectors we found to span the center eigenspace.

Given $\mathbf{W}$ which gives an orthonormal basis for the 4-dimensional subspace of least costly state deviations for a controlled forced periodic structure, as well as $\mathbf{C}$ which gives an orthonormal basis for the center eigenspace of the periodic reference trajectory, we can analyze the difference in the two subspaces. From Stewart's Corollary 2.6,[20] the sine of the largest angle between subspaces is given as the induced 2-norm (largest singular value) of the difference in the projectors onto both subspaces:

$$\sin\theta_{\max} = \|\mathbf{W}\mathbf{W}^T - \mathbf{C}\mathbf{C}^T\|_2 \tag{51}$$

Intuitively a maximal principal angle between subspaces of 90° indicates that there are elements of one subspace that orthogonal to the other subspace. On the other hand, a very small angle indicates close alignment between the two subspaces. In the example case, we see a principal angle difference between these subspaces of... which indicates that these two subspaces align very closely.

Changes to the Period

So far, we have examined forced periodic structures that return to their original state at the same time as the period of the reference orbit about which we conduct our analysis. We may analyze forced periodic structures with an additional small deviation in the return time from the reference period. First, note that if we consider Eq. 14 expanded in terms of variations δt_f in the terminal time t_f, the next term will be third-order overall in δt_f and $\delta\mathbf{y}_0$. As such, we will neglect the first-order contribution of δt_f, and maintain the energy cost quadratic form based on $\delta\mathbf{y}_0$ from Eq. 14 without modification. On the other hand, the final state of the system at time $t_f + \delta t_f$ up to first-order in $\delta\mathbf{y}_0, \delta t_f$ is

$$\delta\mathbf{x}_f = \mathbf{\Phi}_{\mathbf{x}}^{\mathbf{x}}(t_f, t_0)\delta\mathbf{x}_0 + \mathbf{\Phi}_{\boldsymbol{\lambda}}^{\mathbf{x}}(t_f, t_0)\delta\boldsymbol{\lambda}_0 + \frac{d}{dt}\mathbf{x}(t_f)\delta t_f \tag{52}$$

where the additional term can be interpreted as an Euler approximation of the motion at the terminal location of the reference orbit using the vector field at that point. Given this linear approximation, we can solve for the initial costates for a forced periodic structure that starts and ends at offset $\delta\mathbf{x}$

from the reference periodic orbit over a time-of-flight equal to the reference periodic orbit plus the variation in time δt_f:

$$\delta \boldsymbol{\lambda}_0 = \left(\boldsymbol{\Phi}^{\mathbf{x}}_{\boldsymbol{\lambda}}(t_f, t_0)\right)^{-1} \begin{bmatrix} \mathbf{I}_6 - \boldsymbol{\Phi}^{\mathbf{x}}_{\mathbf{x}}(t_f, t_0) & -\frac{d}{dt}\mathbf{x}(t_f) \end{bmatrix} \begin{bmatrix} \delta \mathbf{x} \\ \delta t_f \end{bmatrix} \tag{53}$$

So, the energy cost of a forced periodic structure with a small variation from the reference period can be described using the following 7-dimensional quadratic form:

$$J = \begin{bmatrix} \delta \mathbf{x} \\ \delta t_f \end{bmatrix}^T \underbrace{\mathbf{G}^T \left(\int_{t_0}^{t_f} \left(\boldsymbol{\Phi}^{\boldsymbol{\lambda}_v}_{\mathbf{y}} \right)^T \left(\boldsymbol{\Phi}^{\boldsymbol{\lambda}_v}_{\mathbf{y}} \right) dt \right) \mathbf{G}}_{\mathbf{E}^t} \begin{bmatrix} \delta \mathbf{x} \\ \delta t_f \end{bmatrix} \tag{54}$$

where

$$\mathbf{G} = \begin{bmatrix} \mathbf{I}_6 & \mathbf{0}_{6\times 1} \\ \left(\boldsymbol{\Phi}^{\mathbf{x}}_{\boldsymbol{\lambda}}\right)^{-1} \left(\mathbf{I}_6 - \boldsymbol{\Phi}^{\mathbf{x}}_{\mathbf{x}}\right) & -\left(\boldsymbol{\Phi}^{\mathbf{x}}_{\boldsymbol{\lambda}}\right)^{-1} \frac{d}{dt}\mathbf{x}(t_f) \end{bmatrix} \tag{55}$$

Alternative Definition

We now enforce the relationship $\delta \mathbf{x}(t_f + \delta t) = \delta \mathbf{x}(t_0)$ and

$$\delta \mathbf{x}(t_f + \delta t) = \underbrace{\boldsymbol{\Phi}^{\mathbf{x}}_{\mathbf{x}}(t_f, t_0)\delta \mathbf{x}_0 + \boldsymbol{\Phi}^{\mathbf{x}}_{\boldsymbol{\lambda}}(t_f, t_0)\delta \boldsymbol{\lambda}_0}_{\text{Propagates to } t_f} + \underbrace{\frac{d}{dt}\left(\delta \mathbf{x}(t_f)\right) \delta t_f}_{\text{Euler approx.}} \tag{56}$$

We then must evaluate what $\frac{d}{dt}\left[\delta \mathbf{x}(t_f)\right]$ is

$$\frac{d}{dt}\left[\delta \mathbf{x}(t_f)\right] = \frac{d}{dt}\left[\boldsymbol{\Phi}^{\mathbf{x}}_{\mathbf{y}}(t_f, t_0)\right] \delta \mathbf{y}(t_0) \tag{57}$$

The derivative of $\boldsymbol{\Phi}^{\mathbf{x}}_{\mathbf{y}}(t_f, t_0)$ satisfies the equation

$$\frac{d}{dt}\left[\boldsymbol{\Phi}^{\mathbf{x}}_{\mathbf{y}}(t_f, t_0)\right] = \mathbf{A}(t_f)\boldsymbol{\Phi}^{\mathbf{x}}_{\mathbf{y}}(t_f, t_0) \tag{58}$$

and $\mathbf{A}(t_f)$ is given by linearizing the equations of motion of the reference trajectory at time t_f. This linearization is then

REFERENCES

[1] C. R. McInnes, A. J. C. McDonald, J. F. L. Simmons, and E. W. MacDonald, "Solar sail parking in restricted three-body systems," *Journal of Guidance, Control, and Dynamics*, Vol. 17, No. 2, 1994, pp. 399–406, 10.2514/3.21211.

[2] M. Y. Morimoto, H. Yamakawa, and K. Uesugi, "Artificial Equilibrium Points in the Low-Thrust Restricted Three-Body Problem," *Journal of Guidance, Control, and Dynamics*, Vol. 30, No. 5, 2007, pp. 1563–1568, 10.2514/1.26771.

[3] S. Baig and C. R. McInnes, "Artificial Three-Body Equilibria for Hybrid Low-Thrust Propulsion," *Journal of Guidance, Control, and Dynamics*, Vol. 31, No. 6, 2008, pp. 1644–1655, 10.2514/1.36125.

[4] A. Cox, K. C. Howell, and D. C. Folta, "Dynamical structures in a low-thrust, multi-body model with applications to trajectory design," *Celestial Mechanics and Dynamical Astronomy*, 2019, 10.1007/s10569-019-9891-7.

[5] A. Cox, K. C. Howell, and D. C. Folta, "Trajectory Design Leveraging Low-Thrust, Multi-Body Equilibria and their Manifolds," *Journal of Astronautical Sciences*, 2020, 10.1007/s40295-020-00211-6.

[6] M. Morimoto, H. Yamakawa, and K. Uesugi, "Periodic Orbits with Low-Thrust Propulsion in the Restricted Three-body Problem," *Journal of Guidance, Control, and Dynamics*, Vol. 29, No. 5, 2006, pp. 1131–1139, 10.2514/1.19079.

[7] L. DeLeo and M. Pontani, "Low-Thrust Orbit Dynamics and Periodic Trajectories in the Earth–Moon System," *Aerotecnica Missili and Spazio*, 2022, 10.1007/s42496-022-00122-9.

[8] S. Baig and C. R. McInnes, "Artificial halo orbits for low-thrust propulsion spacecraft," *Celestial Mechanics and Dynamical Astronomy*, 2009, pp. 321–335, 10.1007/s10569-009-9215-4.

[9] A. Tsuruta, M. Bando, S. Hokamoto, and D. J. Scheeres, "New Equilibria and Dynamic Structures Under Continuous Optimal Feedback Control," *Journal of Guidance, Control, and Dynamics*, Vol. 0, No. 0, 2024, pp. 1–12, 10.2514/1.G008270.

[10] C. Sandel and R. Sood, "Natural and Forced Spacecraft Loitering in a Near Rectilinear Halo Orbit," *Journal of Astronautical Sciences*, Vol. 71, 2024, 10.1007/s40295-024-00446-7.

[11] J. Kulik, M. Zweig, and D. Savransky, "Comparing Relative Reahcable Sets About Nearly Circular Orbits," *AAS/AIAA Astrodynamics Specialist Conference*, 2024.

[12] A. E. Bryson, *Applied optimal control: optimization, estimation and control*. Routledge, 2018.

[13] S. Lee and I. Hwang, "Reachable set computation for spacecraft relative motion with energy-limited low-thrust," *Aerospace Science and Technology*, Vol. 77, 2018, pp. 180–188.

[14] H. Sun and J. Li, "Analysis on reachable set for spacecraft relative motion under low-thrust," *Automatica*, Vol. 115, 2020, p. 108864.

[15] J. Kulik, W. Clark, and D. Savransky, "State Transition Tensors for Continuous-Thrust Control of Three-Body Relative Motion," *Journal of Guidance, Control, and Dynamics*, Vol. 46, No. 8, 2023, pp. 1610–1619, 10.2514/1.G007311.

[16] "numpy.linalg.eigh — NumPy v2.1 Manual," 2024. Accessed: December 19, 2024.

[17] J. R. V. Aken, "A Fast Parametric Ellipse Algorithm," *CoRR*, Vol. abs/2009.03434, 2020, 10.48550/arXiv.2009.03434.

[18] "scipy.optimize.minimize — SciPy v1.10.1 Reference Guide," 2024. Accessed: December 19, 2024.

[19] C. Davis and W. M. Kahan, "The rotation of eigenvectors by a perturbation. III," *SIAM Journal on Numerical Analysis*, Vol. 7, No. 1, 1970, pp. 1–46.

[20] G. W. Stewart, "Error and perturbation bounds for subspaces associated with certain eigenvalue problems," *SIAM review*, Vol. 15, No. 4, 1973, pp. 727–764.